6

Spectral Low Coherence Interferometry: A Complete Analysis of the Detection System and the Signal Processing

Eneas N. Morel and Jorge R. Torga
Universidad Tecnológica Nacional, Facultad Regional Delta
Campana, Buenos Aires
Argentina

1. Introduction

Low coherence interferometry (LCI) is an optical technique in which light is used as an instrument to obtain high resolution optical images in a great diversity of materials. It is possible to find in the literature, a variety of configurations with different names, based on the same principle: low coherence reflectometry (OLCR), optical coherence tomography (OCT), white light interferometry (WLI), are only some examples of this. The main idea of this technique is to measure the echo time delay of backscattered light in the sample through the characterization of the interference intensity obtained when the light coming from the sample and the light reflected in a reference surface overlap. When a low coherence source is used, the interference signal is temporally and spatially localized, so it is possible to use this property to obtain distance values or parameters related to the time of flight of the light, reflected in different sections of a sample.

LCI has been proposed and studied since the beginning of the optical science. However, for the last 20 years, there has been a dramatically increase in its applications, mainly due to the development of optical coherence tomography and the evolution of new light sources. The first works of in- surface and optical material characterization was reported in 1960. In 80´s some applications in fibre optics characterization (Takada et al, 1987), topography surfaces and internal structures in transparent media (Youngquist et al, 1987) were proposed with a LCI set-up. It is generally accepted that first biological application was reported by (Fercher, 1988). After these first works, optical coherent tomography (OCT) became a powerful technique for medical diagnosis, (Huang, 1991), in which images of the human retina and coronary artery were obtained. Since then, OCT has evolved, and nowadays it is a well-established technique for ophthalmic diagnosis and other biological tissues (Brezinski, 2006).

New developments in light sources, fibre optic elements, detectors and processing techniques allow a dramatic increase in resolution and speed of image acquisition. These advances transform this technique in a powerful three-dimensional visualization method which has a wide diversity of applications. Over the last ten years its growth has been explosive; proof of this is the increasing number of publications, patents and companies involved in this subject (www.octnews.org). There is no doubt that this evolution has been

the result of the numerous successful OCT applications in the medical field, especially in ophthalmology (Drexler et al, 2008). Over the last years its application in material characterization and non-destructive techniques is another field that is growing fast (Goode, 2009). Micro structures and MEMS characterization, surface topography, structural parameters in semitransparent materials, analysis and visualization of structural vibrations, are only a few examples (Bruce et al, 1991), (Wiesauer et al, 2005), (Wiesner et al, 2010).

Nowadays, there are several companies that offer commercial systems based on this tecnique. Polytec®, Thorlabs®, Carl Zeiss® are only some examples. Figure 1 show an image obtained with the Stratus from Carl Zeiss®. This equipment is capable of exploring the eye at a speed of several thousand lines per second.

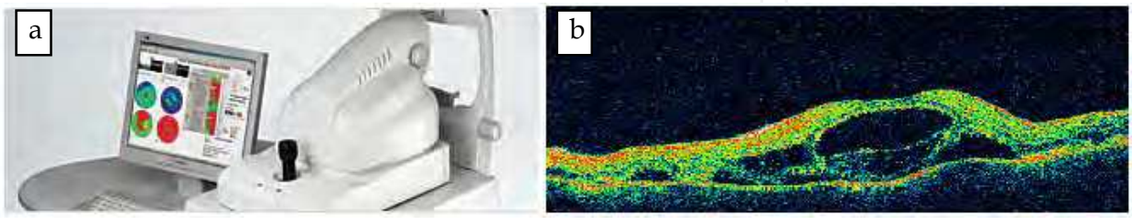

Fig. 1. a) Stratus 3000 Carl Zeiss®. b) OCT image of retina, taken with Stratus 3000 (Michael P Kelly, Duke Eye Imaging, Duke University Eye Center, Durham, NC). Photos used with permission of Carl Zeiss®.

Another example is shown in figure 2; TSM-1200 TopMap® µ.Lab from Polytec® that can be used to acquire high-resolution topographical maps of functional surfaces and microstructures.

Fig. 2. TMS-1200 TopMap µ.Lab. Photos used with permission of Polytec®.

High-speed 3D OCT imaging can provide comprehensive data that combines the advantages of optical coherence tomography and microscopy in a single system. Shown below are some 3D image data sets of two samples; in figures 4 it is shown how this technique can obtain the surface topography of a screw.

Fig. 3. 3D optical profiling of an M2 metal screw. Photos used with permission of Thorlabs®.

In figure 4 it is shown a tomography of a finger skin.

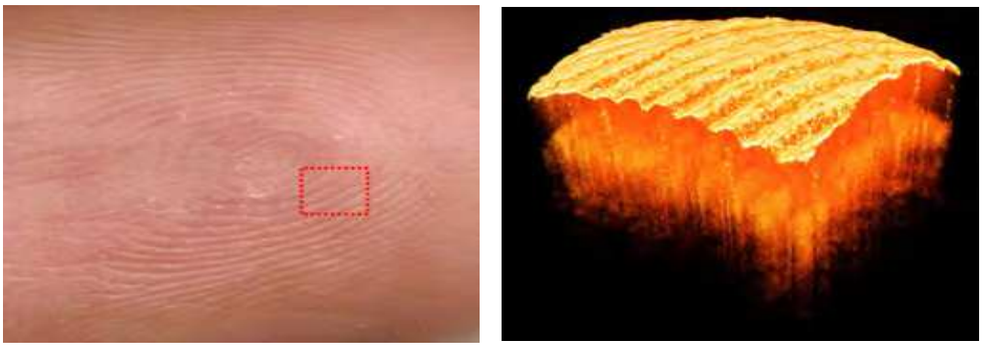

Fig. 4. Human finger pad. Photos used with permission of Thorlabs®.

1.1 Basis of low coherence Interferometry

Interference can be considered as the wave pattern that is obtained after the superposition of two or more waves. In low coherence interferometry, superposition is obtained with a broadband light source, and the wave pattern in this situation is considerably different from that obtained with a standard monochromatic source. (Born, M. & Wolf, E., 1999).

In interferometry techniques the interference signal is usually obtained from the superposition between light backscattered from a reference arm and a sample arm as it is shown in figure 5 below.

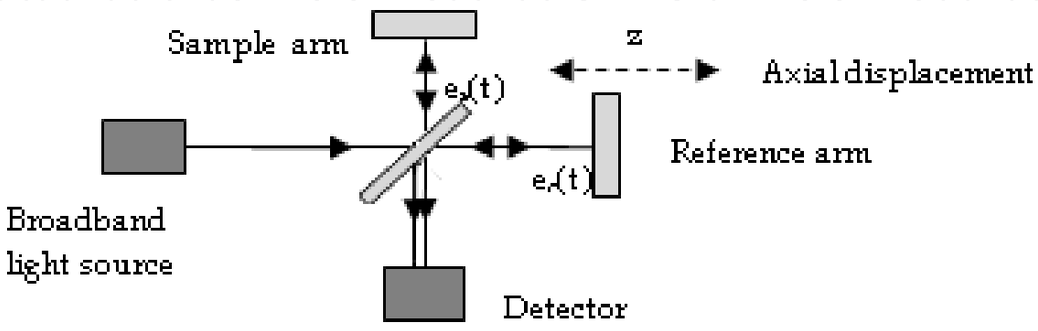

Fig. 5. Michelson interferometer set-up.

The total intensity at the detector at a time t, is obtained as the superposition of $e_r(t) = Re(Er(t))$ and $e_s(t) = Re(E_s(t+\tau))$, the electric field from the reference and from the sample respectively. $Re(E(t))$, indicates the real part of the complex expression of the electric field, $E(t)$. τ is the difference in time of flight of light in each arm and it is a consequence of the different optical path length. The symbol < > indicates temporal average, K is a constant factor.

$$I = K\left\langle \left| E_r + E_s \right|^2 \right\rangle = I_r + I_s + 2K\langle \mathrm{Re}(E_r(t+\tau)E_s(t)) \rangle \tag{1}$$

The reflectivity in the interface at the end of the reference and the sample arm are considered by the coefficient R, which is assumed constant. If Io is the intensity at the output of the light source, the intensity of each arm after the reflections is: $I_r = R_r I_o$ and $I_s = R_s I_o$. Then, equation 1 can be written:

$$I = R_r I_o + R_s I_o + 2\sqrt{R_s R_r}\,\mathrm{Re}(\Gamma(\tau)) \tag{2}$$

In the last term in equation 2, usually named the interference term, the complex coherence function $\Gamma(\tau) = K\langle E_o(t)\, E_o(t+\tau)\rangle$ is defined (Goodman, 1984); that is the correlation of the electric field. This function is closely related to the concept of coherence time -T - a measure of the delay between two beams which is necessary to blur the interference term. A useful way to define this concept is (Goodman, 1984):

$$T = \frac{1}{\left|\Gamma(0)\right|^2} \int_{-\infty}^{\infty} \left|\Gamma(\tau)\right|^2 \, d\tau \tag{3}$$

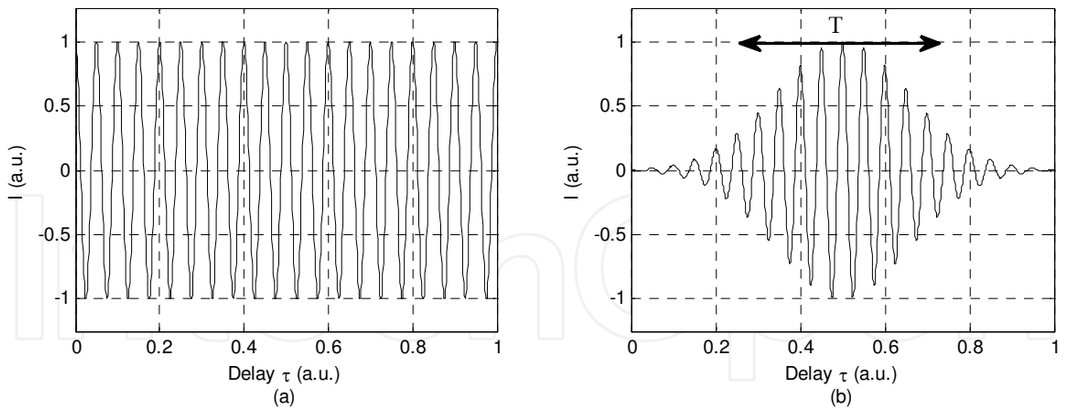

Fig. 6. Total intensity (I), as a function of time delay(τ) for a coherent source a) and for a low coherence source b).

It is possible to illustrate this concept -close to the basic idea of low coherence interferometry- considering the total intensity I as a function of τ, the time delay. To do this, we perform an axial scan of the reference sample. In the simplified interferometer scheme of figure 5 this can be done with a movement of the reference surface with a constant velocity (axis z figure 5).

When the light source is monochromatic, the total intensity shows the same variation (figure 6-a). Using a low coherence source, interference is only observed when the path length is within the coherence length of the light source (figure 6-b).

1.2 Experimental configurations

We will show a generic system of low coherence interferometry with a brief description of the experimental set-up and the function of each component. The general configuration can be separated in four well differentiated sections: the broadband light source, the interferometer, the sample with its holder and the detection system.

Figure 7 shows the basic set-up used in most of the low coherence applications. The initial system is the broadband light source [1], that is a critical factor since an appropriate selection in its characteristics is crucial in the final quality of the images obtained (Drexler et al, 2008). Nowadays there is an important offer of broadband sources with different center wavelengths, power, and beam quality (stability, noise, single transverse mode, etc.).

Diode systems are probably the most utilized light sources, as the superluminiscent LED`s (SLD). They have the advantage to be easy to hand and operate; also, their spatial dimension is reduced, their price is usually lower than other systems, and they are appropriated for no-laboratory applications. Amplified spontaneous emission (ASE) sources are an interesting alternative as they offer a broad bandwidth in the infrared region. Finally there is a group based on ultra-short laser pulses and supercontinuum light sources which is an attractive option as it offers high power, broad bandwidth and good quality in spatial mode. These systems are expensive comparatively.

The output beam from the source is directed to the interferometer. There is a great variety of configurations proposed in the literature, but in most of these works a Michelson type is used (Schmitt et al, 1999). A typical configuration is shown in figure 7. The output beam is split in the beamsplitter [4]. One of the beams goes to the reference surface [2]-usually a mirror- and the other beam goes to the sample [3]. After the reflection on each surface, both beams are sent to the detector [5]. The superposition generates the interference signal.

With this signal it is obtained a measurement of the OPD between both arms. In most cases the light beam is focused on the sample so that the measurement process is performed point to point on the desired region. For opaque samples, the light is reflected only on the surface, so a topography measurement is obtained. For transparent or semi-transparent media, light is reflected from sub-surface structures in the sample, so a tomography measurement is performed.

Usually the sample-holder or the light beam can be displaced in a 2-D lateral movement (axis x and y in the figure 7). This way the sample can be inspected in the region of interest.

Although there are many configurations proposed based on the general configuration described before, it is possible to make a division into three main groups, each one with its particular characteristics. They are commonly known as:

1. Time domain low coherence interferometry (TDLCI)
2. Spectral domain low coherence interferometry (SDLCI)
3. Sweep source domain low coherence interferometry (SSDLCI)

In TDLCI mode the total interference is obtained with a one element detector([5] in figure 7), usually a photodiode, and the total intensity is registered while the optical path of the reference arm changes from a maximum to a minimum value that is predefined for each set-up (displacement in the z direction – figure 7). While the reference arm is moving the sample is maintained in the same position (Drexler et al, 2008).

In SDLCI mode the detection [5] is performed with a spectrometer. In this scheme the interference signal is obtained with the superposition of the spectral intensity of both arms. (Drexler et al, 2008).

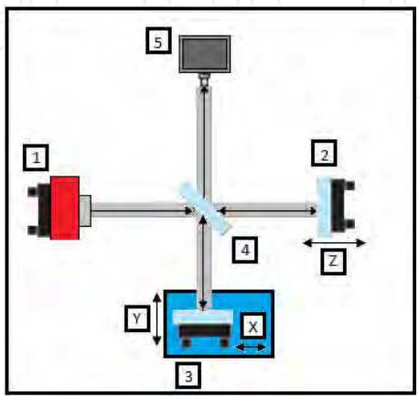

Fig. 7. A typical low coherence interferometry experimental set-up.

Based on the same idea, in the SSDLCI configuration, a tuneable laser and a one element photodetector are used. The light source is swept in wavelength as a function of time, so the spectral components are not encoded by spatial separation, they are encoded in time. After a complete swept we obtain the spectrum one by one wavelength (Choma et al 2003), and consequently the interference signal.

2. Spectral domain low coherence interferometry

2.1 Introduction

Spectral domain low coherence interferometry (SDLCI) -also known as Fourier domain low coherence interferometry (FDLCI)- is, as mentioned before, one of the configurations commonly used in low coherence interferometry. The first result using this technique (Fercher et al, 1995) was for ophthalmological measurements and some years later (Hasler et al, 1998) in dermatological applications. After these initial works, it began to be shown as a competitive technique with the time domain method (TD-OCT), a well established method for optical coherence tomography (OCT) applications at that time. Since then, SDLCI has shown several advantages which have favoured its development and the high level of acceptance that it has nowadays.

These advantages can be summarized in the lack of need for a fast mechanical scanning mechanism (Drexler et al, 2008) that brings the simplicity of no moving parts in the reference arm of the interferometer, and the superior sensitivity of the detection (Leitgeb et al, 2003). The SDLI typical configuration is shown in figure 8. The light source and the interferometer scheme follow the same characteristics described before, but the detection system is a distinct point in this technique. The main idea is that the optical path difference

between the sample and the reference is obtained from the analysis of the superposition of the spectrum of the light source reflected in each arm of the interferometer. This spectrum is commonly measured with a spectrometer. Most of the detection systems employ linear arrays as a sensor element. Some works with 2-D CCD systems and individual processing of each pixel, has been already presented (Vakhtin et al, 2003).

Figure 8 below illustrates the basic experimental set-up assuming a simple situation in which there are only two reflections, one at the end of each of the arms of the interferometers. The interference signal is measured with the spectrometer sensor where the total intensity is obtained as a function of the wavelength *(λ)*.

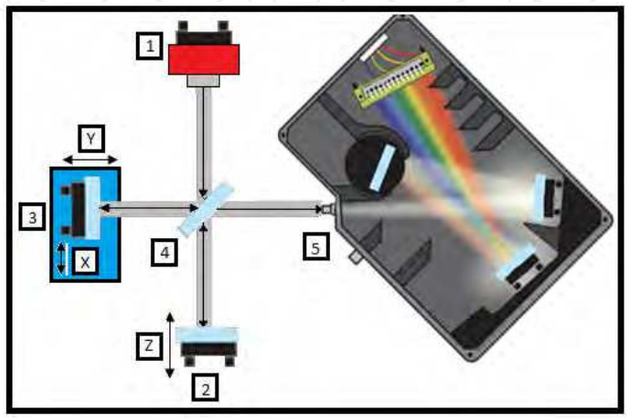

Fig. 8. A typical spectral doamin low coherence interferometry experimental set-up.

2.2 The interference signal and the detection system

It is assumed that $I_o(k)$ encodes the power spectral dependence of the light source ([1] in figure 8), were $k=2\pi/\lambda$, is the wavenumber. The interference fringes surges from the superposition of the spectrum of the light coming from the two reflections. We call $I_{r1}(k)$ to the intensity coming from the reference arm and $I_{s1}(k)$ to the intensity coming from the sample arm . The expression for the total intensity is then:

$$I(k) = I_{r1}(k) + I_{s1}(k) + 2\sqrt{I_{r1}(k)I_{s1}(k)}\cos\left(k\Delta x_{r1s1}\right) \tag{4}$$

The first two terms are known as DC intensities in the literature (Drexler et al, 2008). The last term in equation 4 is the interference component, and it includes the OPD dependence that, in this simple situation, is given by the value $\Delta X_{r1s1} = x_{r1}-x_{s1}$, where x_{r1} and x_{s1} are the total path length in each arm, both measured from the beamsplitter.

To simplify the expression, we use $\beta^2 = R_{s1}/R_{r1}$, the reflectivity coefficients ratio, and it is assumed that these coefficients have no dependence on the wavenumber, that is: $I_{r1}(k) = R_{r1}I_o(k)$ and $I_{s1}(k) = R_{1s}I_o(k)$, as mentioned in equation 5, so:

$$I(k) = R_{r1}I_o(k)\left(1+\beta^2+2\beta\cos\left(k\Delta x_{r1s1}\right)\right) \tag{5}$$

The figure 9 shows an example of an image obtained in a 2D-CCD sensor at the end of the spectrometer (see set-up picture). The image corresponds to the total intensity described

before in equation 4. In this particular example, the source is a superluminescent diode (λo = 840 nm, Δλ = 20nm) and $R_{1s} = R_{1r} \approx 0.08$.

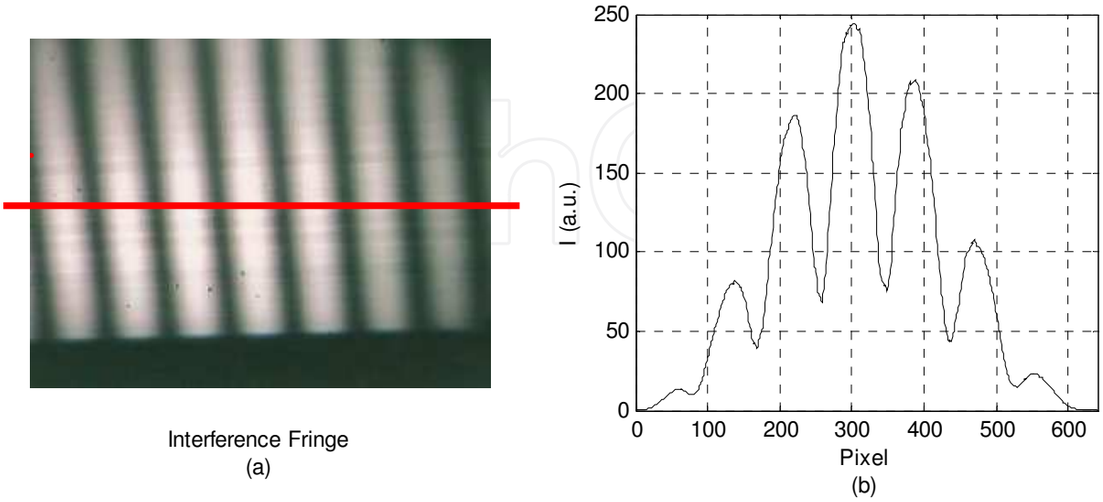

Fig. 9. a) Interferences fringes obtained with a 2-D spectrometer sensor b) Intensity as a function of k obtained from a row of pixel from the image a).

Figure 9-b represents total intensity, obtained from a line of pixels of the image shown in figure 9-a. The modulation in the curve is produced by the interference term over the Gaussian spectrum of the light source.

In a general situation in which it is assumed that there are several reflections in the reference arm and in the sample arm, the total intensity expression can be written as:

$$I(k) = \sum_{i=1}^{N} I_i(k) + \sum_{i,j=1}^{N} 2\sqrt{I_i(k) I_j(k)} \cos\left(\Delta x_{ij}\right) \tag{6}$$

N represents the total number of reflectors in the sample and in the reference. The sub index i or j identifies the region where the reflection is produced in the reference (r_1, r_2, r_3, …) or in the sample arm (s_1, s_2, s_3, …). To illustrate this point, we show a typical application in which the reference arm is a mirror (1r) and the sample is a slab in air. The slab has two interfaces (1s and 2s), an inner group index *n*, and a thickness *d*.

$$\begin{aligned} I(k) = {} & I_{r1}(k) + I_{s1}(k) + I_{s2}(k) \\ & + 2\sqrt{I_{r1}(k) I_{s1}(k)} \cos\left(\Delta x_{r1s1}\right) \\ & + 2\sqrt{I_{r1}(k) I_{s2}(k)} \cos\left(\Delta x_{r1s2}\right) \\ & + 2\sqrt{I_{s1}(k) I_{s2}(k)} \cos\left(\Delta x_{s1s2}\right) \end{aligned} \tag{7}$$

The first three terms are the DC terms mentioned before. The second and the third term correspond to the cross correlation between the reference and each of the sample surfaces; the forth term is the correlation component that surges from the reflections on both interfaces of the sample. (see figure 10).

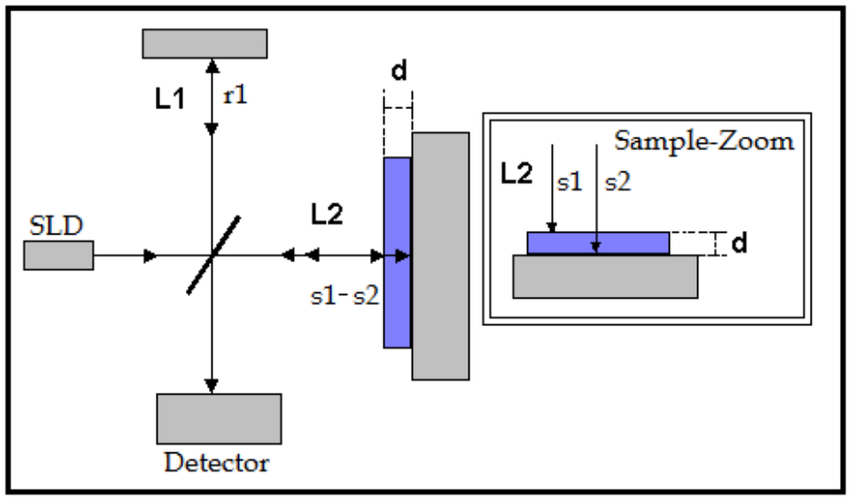

Fig. 10. Experimental set-up for thickness measurement of a slab.

So in this situation the OPD values in equation 7 are: $\Delta x_{r1s1} = x_{r1} - x_{s1}$, $\Delta x_{r1s2} = x_{r1} - (x_{s1} + 2.\ n.d)$ and $\Delta x_{s1s2} = 2.n.d$. Where x_{s1}, x_{s2}, x_{r1} and 2.nd, are the total optical path distances corresponding to each interface indicated in figure 10.

The usual way to obtain the OPD values from the total intensity data is to apply the Fourier transform. We call *FI(x)* to the Fourier Transform of *I(k)*, where x is the conjugate variable of the wavenumber *k*.

As an example it is shown the expression for *FI(x)* in the situation mentioned before (equation 4), where the interference signal is obtained from only two reflections (r_1 and s_1). So:

$$FI(x) = F(I_0(k)) \otimes F\left(R_{r1} + R_{s1} + 2\sqrt{R_{r1}R_{s1}}\cos(\Delta x_{r1s1}k)\right) \tag{8}$$

We denote the convolution as ($\otimes$).

According to the Wiener–Kinchin theorem (Goodman, 1984), the first term in the convolution is the coherence function $\Gamma(x)$ and the second term yields two delta functions located at $\pm\Delta x_{r1s1}$ (Papoulis, 1962).

Therefore, the last expression can be written as:

$$\begin{aligned} FI(x) &= \alpha.\Gamma(x) \otimes \\ &\left[\delta(x)(R_{r1} + R_{s1}) + 2\sqrt{R_{s1}R_{r1}}\left(\delta(x - \Delta x_{r1s1}) + \delta(x + \Delta x_{r1s1})\right)\right] \end{aligned} \tag{9}$$

Being α a constant factor.

Figure 11-a and 11-b illustrate the interference signals in two situations that correspond to different deep modulation *(β = 1, β = 0.5)*. Figures 11-c and 11-d show the absolute value of the corresponding Fourier transform for each signal. This graph shows three "interference peaks". One is centred in the origin of the *x* axis and the "lateral peaks", denoted as P and Q in the figures, are centred in $\pm\ \Delta x_{r1s1}$.

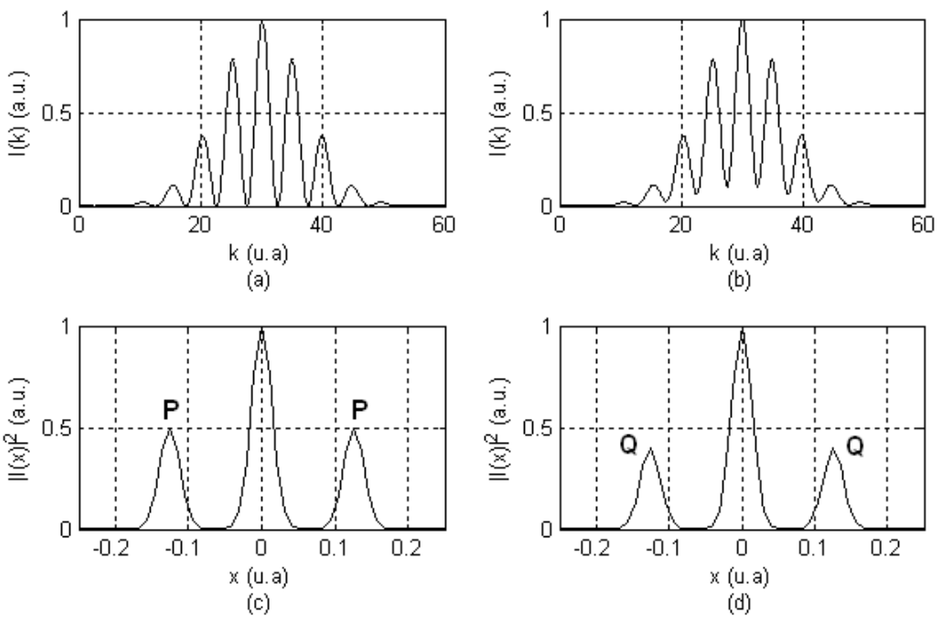

Fig. 11. a) and b) shows the total interference signal as a function of wavenumber k, for two different β relations. c) and d) shows its corresponding Fourier transform as a function of x (the conjugate variable of k) .

Figure 12 shows an example of how the position of the interference peak changes according to the increment of OPD between both arms. The peaks in order zero no contain OPD information.

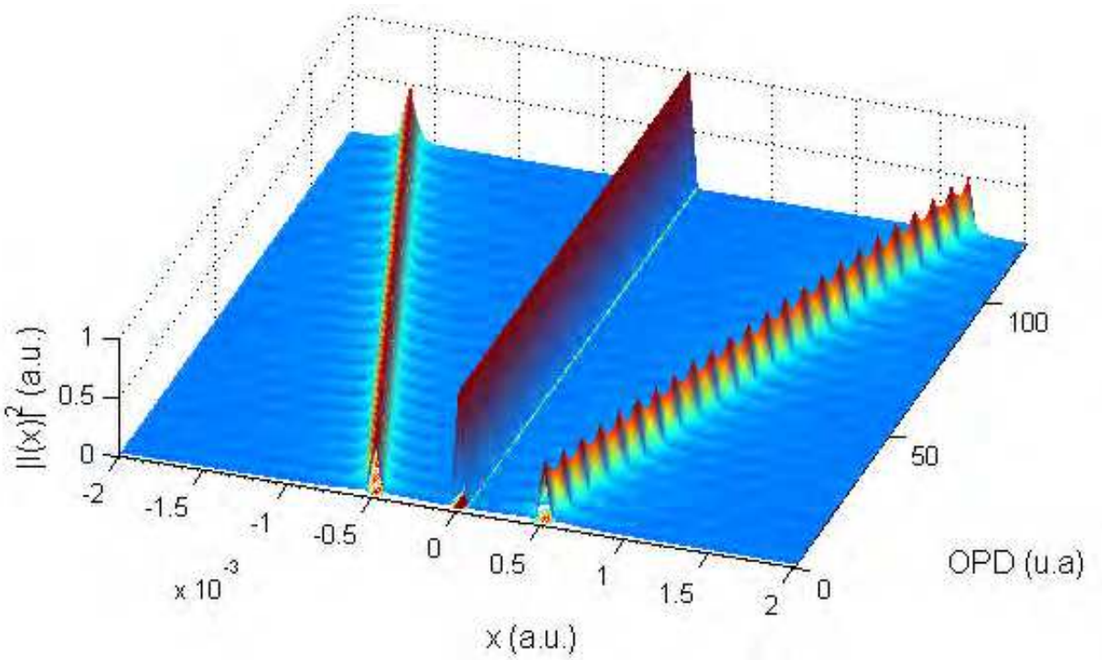

Fig. 12. Interference peak vs OPD increments.

2.3 Signal detection and parameter limits

In an ideal situation, the intensity function *I(k)* would be obtained with a "perfect" spectrometer. In a real situation, it is important to evaluate the spectrometer parameters in order to optimize the measurements and evaluate possible artifacts, errors or limitations introduced for the "real" set-up. We assume a detector model based on a grating spectrometer with a linear array sensor. There are some important issues to be considered in this evaluation, more details can be found in (Hu et al, 2007; Jeon et al, 2011).

a. The spectrometer is used for separating the different wavelengths of the light source spectrum and to focus each of them on the sensor that is considered as a linear array of N_p pixels. After its calibration it is possible to define a *k* axis in the array direction. The spectral range of the spectrometer (Δk_a) is given by the interval $[k_1, k_{Np}]$ where k_1 is the value assigned to the first pixel and k_{Np} to the last one. We also define the "*Range*" function as follows:

$$Range(k) = \prod\left(\frac{k-k_a}{\Delta k_a}\right) \tag{10}$$

k_a indicates the central wavelength in the spectrometer. Along this work we assume $\Pi(z)$ a *rect* function defined as 0 if $|z|>1/2$ and 1 if $|z|<1/2$.

b. The dimensions of the spot of each wavelength focused on the sensor is taken into account by the point spread function (*Psf(k)*) (Hu et al, 2007). The width, the shape and the position of the center of this spot depends on the spectrometer characteristics such as the entrance slit width, diffraction grating and focal length and eventually on the spatial profile of the light source in the spectrometer entrance (Dorrer et al, 2000). We assume a Gaussian shape (Hu et al, 1997) where its FWHM (Δk_{psf}) is a measurement of the spot size.

$$Psf(k) = psf_0.e^{-4\ln(2)\frac{(k-k_i)^2}{\Delta k^2_{psf}}} \tag{11}$$

The " ideal" detected signal is then modified by the convolution with this function:

$$I_r(k) = \int_{-\infty}^{\infty} I(k').Psf(k-k')dk' = I \otimes Psf(k) \tag{12}$$

c. The value obtained in a particular pixel "i" is the total intensity integrated over a width (Δk_{pix}), which is defined by the pixel dimensions, the grating dispersion and the focus length of the spectrometer (Leitgeb et al 2003; Hu et al 2007). This average value can be written as:

$$I_r(k_i) = \int_{-\infty}^{\infty} (I \otimes Psf)(k).Pix(k-ki)dk = I \otimes Psf \otimes Pix(k_i) \tag{13}$$

The convolution takes into account the process described before. A first approach to this function can be to assume a rectangular shape where its width is: $\Delta k_{pix} = \Delta k_a / N_p$ (Hu et al, 2007) (Wang et al, 2008). Here it is assumed by simplicity that the fill factor is 100%.

$$Pix(k-k_i) = \Pi(\frac{k-k_i}{\Delta k_{pix}}) \tag{14}$$

More complex dependence with k can be thought, considering additional effects such as crosstalk or fill factor (Jeon et al, 2011).

d. The measurement of the total intensity $I(k)$ obtained from the detector is a discrete collection of N_p values. Each value corresponds to the average intensity measured in one pixel, for this reason, it is convenient to define a sampling comb of delta functions as (Dorrer et al, 2000):

$$C(k) = \sum_{i=-\infty}^{+\infty} \delta(k-k_i) \tag{15}$$

Where k_i is the value assigned to the pixel with index i (Wang et al,2006); (Hu et al, 2007).

The following figure shows a schematic of the spectrometer sensor and a detail of how two wavelengths (λi and λj) have been focused on it. The picture also shows how the "*pix*" and "*psf*" function combine to define the average value in pixel j.

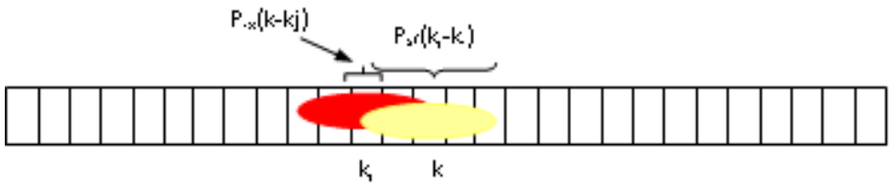

Fig. 13. Schematic of the spectrometer sensor array and the "psf" and "pixel" functions.

Then, the final expression for the signal intensity is:

$$I(k) = Range(k)(C \otimes psf \otimes pixel \otimes I)(k) \tag{16}$$

$$I(k) = \prod(k-k_a) \sum_{i=-\infty}^{\infty} \delta(k-k_i)\left(pixel \otimes psf \otimes I(k)\right) \tag{17}$$

Under these considerations the A scan signal $FI(x)$ is obtained applying the Fourier transform of equation 17. Here the x variable is the conjugated of k.

$$\begin{aligned} FI_4(x) = & F\left(\prod(k-k_a)\right) \\ & \otimes F\left(\sum_{i=-\infty}^{\infty} \delta(k-k_i)\right) \\ & \otimes \left(F(pixel(k))F(psf(k))F(I(k))\right) \end{aligned} \tag{18}$$

That can be written as:

$$FI(x) = FI_0 \sin c\left(\frac{\Delta k_a}{2}x\right) \otimes \sum_{n=-\infty}^{\infty} \delta(x - n\Delta x) \otimes \left[\sin c\left(\frac{\Delta k_{\boldsymbol{pix}}}{2}x\right).\exp\left(-\frac{\Delta k^2_{psf}x^2}{16\ln(2)}\right)F(I(k))\right] \quad (19)$$

This expression is easily obtained from equation 18 and some mathematics relations (Papoulis, 1969). FI_o is a constant factor that also absorbs all the pure phase terms that result from the Fourier transform. The new delta comb has a period $\Delta x=2\Pi/\Delta k_{pix}$, the interval available for signal processing avoiding aliasing.

The expression in brackets in equation 19, shows the Fourier transform of the "ideal." intensity and the modifications introduced by the Fourier transform of the *psf* and the *pixel* function.

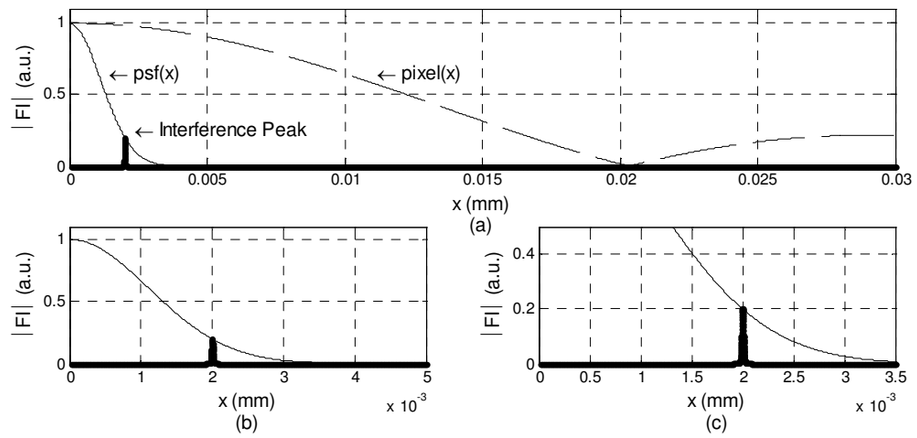

Fig. 14. a) Interference peak and the psf and pixel Fourier Transform functions. b) and c) Zoom of figure a).

This modification means a sensitivity fall-off when the OPD value increase. In the figure 14 it is shown these terms for a typical situation.

As it can be appreciated from the figure 14, the shape of both functions (the *sinc* and *psf* Fourier transform) generate a decrease in the visibility amplitude of the interference peak that goes to zero when x increase. So, there are two parameters that limit the dynamic range of the technique. One is: $x_{pix}=2\pi/\Delta k_p$, the first zero of the *sinc* function. The other is the FWHM of the Gaussian function obtained as the Fourier transform of the *psf*: $x_{psf}=4.\ln(2)/\Delta k_{psf}$ (Bajraszewski et al, 2008), (Leitgeb et al, 2003).

2.4 Signal processing

In the last section we showed some considerations in the interference image, imposed by the real characteristics of the detector. The SDLCI detection process ends with an array of N_p

data points that contain the information of the depth profile of the sample. This process usually continues with the analysis of the Digital Fast Fourier Transform (FFT) of this vector. The classical algorithm is shown in equation 20, where N_p is the I[n] length.

$$FI[q] = \sum_{n=0}^{N_p-1} I[n] W_{N_p}^{qn} \quad / \quad W_{N_p}^{qn} = e^{-j\left(\frac{2\pi}{N_p}\right)} \tag{20}$$

In figure 15 a typical example is shown. The interference signal is registered in a 640-point array (figure 15-a). Its conventional FFT is shown in figure 15-b. The interference spectrum has been obtained in a wavelength range from 780 to 880 nm. The modulation corresponds to a situation in which there is only one surface (*r1* and *s1*) in both arms of the interferometer, as presented in equation 4.

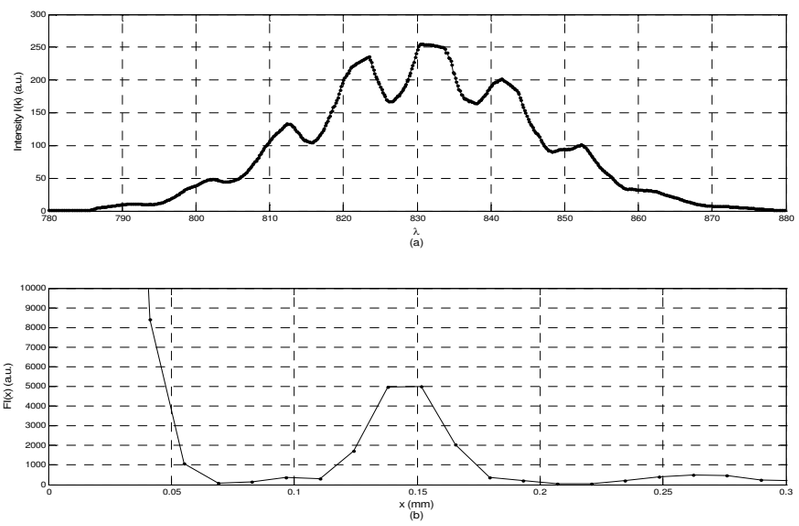

Fig. 15. a) Interference signal and b) Interference peak.

The OPD value Δx_{r1s1} in this scheme is the abscissa coordinate of the maximum point of the lateral peak in the Fourier transform curve (figure 15-b). With the conventional Cooley-Tukey FFT algorithm the sampling interval is:

$$\Delta x_{samp} = \frac{2\pi}{N_p \Delta k_{pix}} \tag{21}$$

Where N_p and Δk_{pix} are the parameters previously defined. In this step, spectral calibration is a critical process. First, a conversion of the measured spectrographs from λ-space to k-space is needed. As the spectra obtained by the spectrometer are not necessarily evenly spaced, a posterior resample to be uniformly spaced in k-axis is required. This implies a careful calibration of each pixel of the sensor. There are several works in which this point is presented (Dorrer et al, 2000; Hu et al, 2007) and different experimental and post process arrangements are proposed (Bajraszewski et all, 2008; Jeon et al 2011).

Another point that can be avoided or smoothed by signal processing is the edge effects in the Fourier transform of the *Range* function proposed in equation 10, to take into account the spectrometer range. To modify the shape of the rectangular function the windowing technique can be used (Oppenheim et al, 2000). With this tool it is possible to minimize the effects that result in spectral leakage in the *FI(x)* signal, and to increase the resolution in the OPD measurement.

There are many types of windows available in the literature. Figure 16 shows common functions (Rectangular, Bartlett, Hanning, Hamming, Blackman, Blackman-Harris and Gaussian).

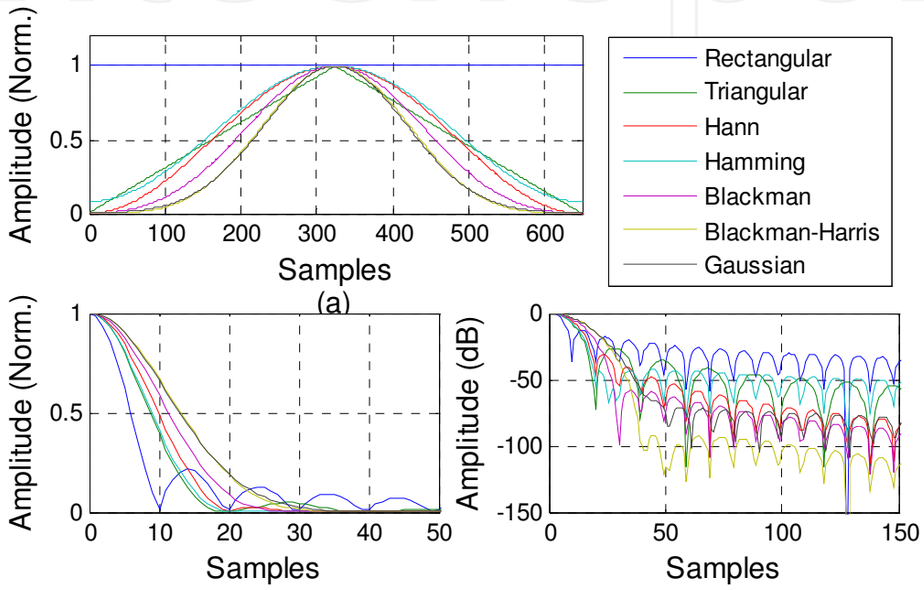

Fig. 16. Typical windows functions and b) the corresponding FFT curves. c)

A spectral analysis of the different window functions is recommended to determine the best to use. In some cases it is possible to apply more than one window simultaneously.

To increment the resolution some techniques can be used (Boaz Porat, 1997). One of the most popular is known as Zero Padding (ZP) (Dorrer et al, 2000; Yun et al, 2003). In this technique the original array *I[k]* is extended with zeros, then, the length of the new array changes to $M_p > N_p$. As a consequence, the sampling interval can be reduced by a N_p/M_p factor with the disadvantages that mean computing longer vectors and more time consuming.

An alternative technique that allows reducing the sampling interval Δx_{samp} in a similar way to ZP but in a localized region of the x axis is the Chirp Fourier Transform (CFT). This predefines the sampling interval and the region of interest on the x axis.

If a sequence I[n] with $0 \le n \le N_p\text{-}1$ is used, we can write the DFT:

$$F\left(\theta[q]\right) = \sum_{n=0}^{N_p-1} I[n] e^{-j\theta[q]} \quad / \quad \theta[q] = \theta_0 + q\Delta\theta, \; 0 \le q \le q-1 \tag{22}$$

Where $\Delta\theta$ is the sampling resolution desired, θ_0 the initial x value and K the number of additional points. Therefore, through θ_0, $\Delta\theta$ and N_p, you can delimit the frequency range in which you want to work. The operation number required is approximately M+N.

In figure 17, the original signal FI[x], FI_{ZP}[x] and FI_{CFT}[x] are shown, the sequence I[k] has 640 points but in the FI[x] only six point defined the interference peak (figure 17-a). To increment the resolution in a factor of 5, we used ZP and CFT. The resolution level is equal in both cases but FI_{ZP}[x] has 3200 points and FI_{CFT}[x] has only 81 points as showed in figure 17-b and 17-c.

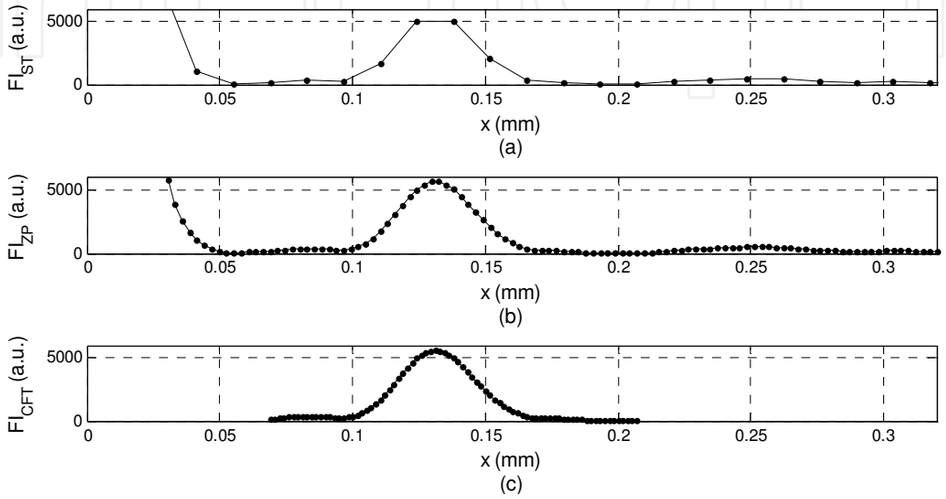

Fig. 17. (a) FI[x], (b) FI_{ZP}[x] and (c) FI_{CFT}[x].

3. Experimental results

In this section we show results obtained from an experimental configuration similar to that presented in section 2.1. The idea is to show that with a relatively simple set-up, it is possible to apply this technique in a variety of applications with interesting results. The light source is a superluminescent infrared diode, centered at 840nm, with a 20- nm bandwidth and a 5-mw output power. The interferometer is a Michelson type, in air , and the detector is a spectrometer Ocean Optics model 4000. With this configuration we get a 2-mm dynamic range and the axial resolution is lower than 10 microns.

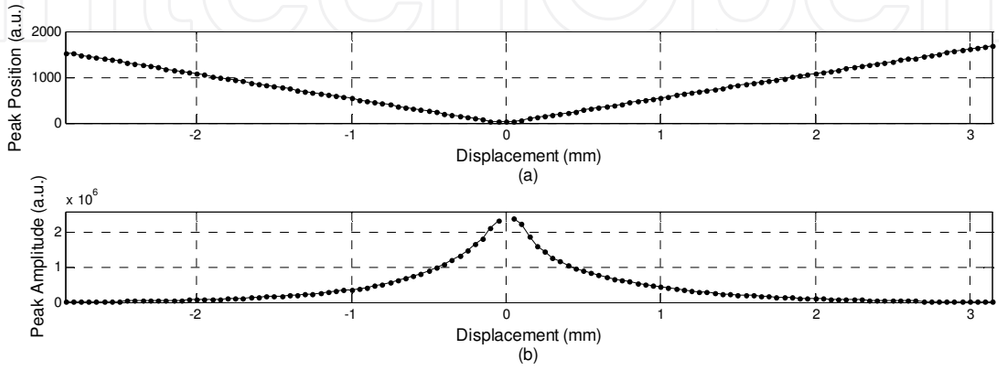

Fig. 18. a) Calibration curve and b) Amplitude variation of interference peak.

At first a calibration process is shown. As it has been mentioned before, it is necessary to link the interferometer signal with the OPD absolute values. A simple way to do this is to move the reference surface through controlled displacements (OPD) or steps, and simultaneously register the abscise coordinate of the center of the FTI peak that corresponds to each step. Figure 18-a shows the peak abscise coordinate (pixel number) versus displacement. Figure 18-b shows the peak amplitude versus the corresponding displacement.

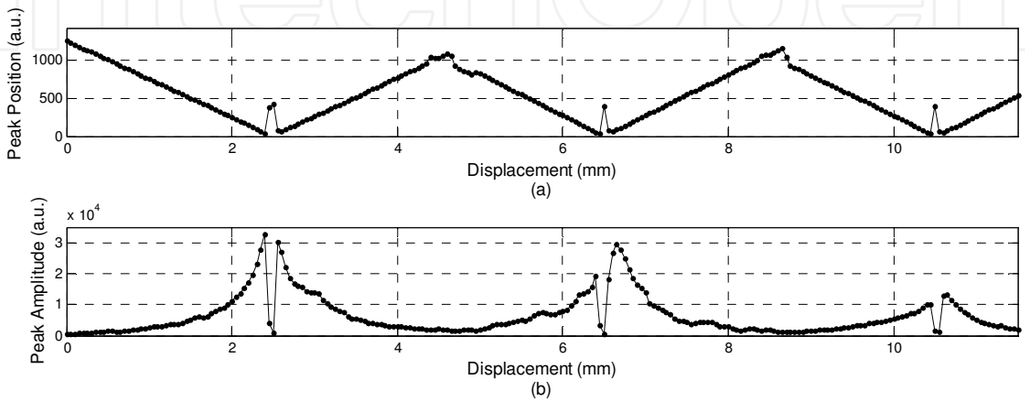

Fig. 19. a) OPD in pixel vs Displacement and b) Amplitud variation of interference peak.

The amplitude fall-off shows the consequence of the "real parameters" of the detector explained in section 2.3. For this particular set-up the *psf* function is predominant.

When the OPD value is close to the limit imposed by Nyquist, aliasing effects can affect the interference signal (Dorrer et al, 2000). If the Nyquist limit is transposed, the measurement shows no-real OPD values that can be misunderstood (figure 19).

In the next example the technique is used to obtain the profile of a metal sample. The sample is a gauge (class 2-norm ISO 3650, model M7T the C.E. Johansson Inc.); its nominal thickness is 1100 ± 0.45µm; this gauge was placed on a second gauge which was used as a reference plane, as shown in figure 20. A 4- mm length profile was obtained on the region indicated in the figure 20 (2 mm on the gauge surface and 2mm on the reference plane).

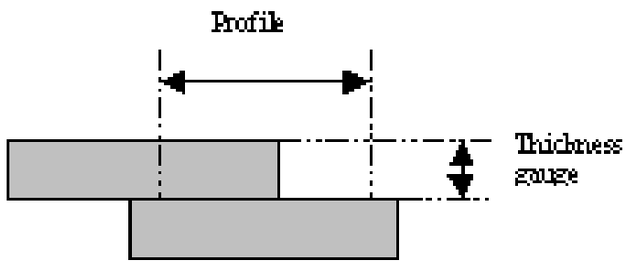

Fig. 20. Schematic of the sample.

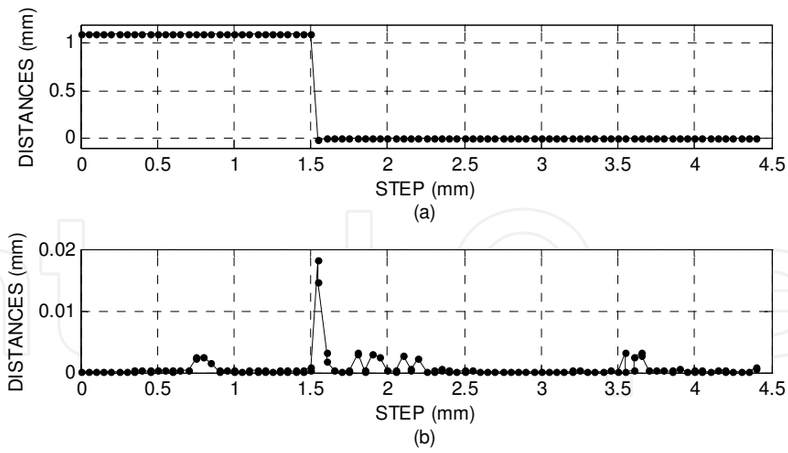

Fig. 21. a) Profile obtained by SDLCI by a sequence of points measured on the sample surface. b) Dispersion in the axial distance measurement.

The profile is obtained by measuring the axial distance in a sequence of points on the sample surface (figure 21-a). Each point is measured after a lateral displacement by steps of 50 microns. The value of gauge thickness obtained from this measurement is: 1100 ± 0.71 µm. Figure 21-b shows the dispersion in each point measured, which is much lower than the coherence length of the source, except on the borders of the sample step.

In the following example an application on 3D- surface measurement is shown. These measurements are critical to the successful manufacturing of precision parts. Components and structures ranging from submillimeter to centimeter size can be found in many fields including the automotive, aerospace, semiconductor and data storage industries.

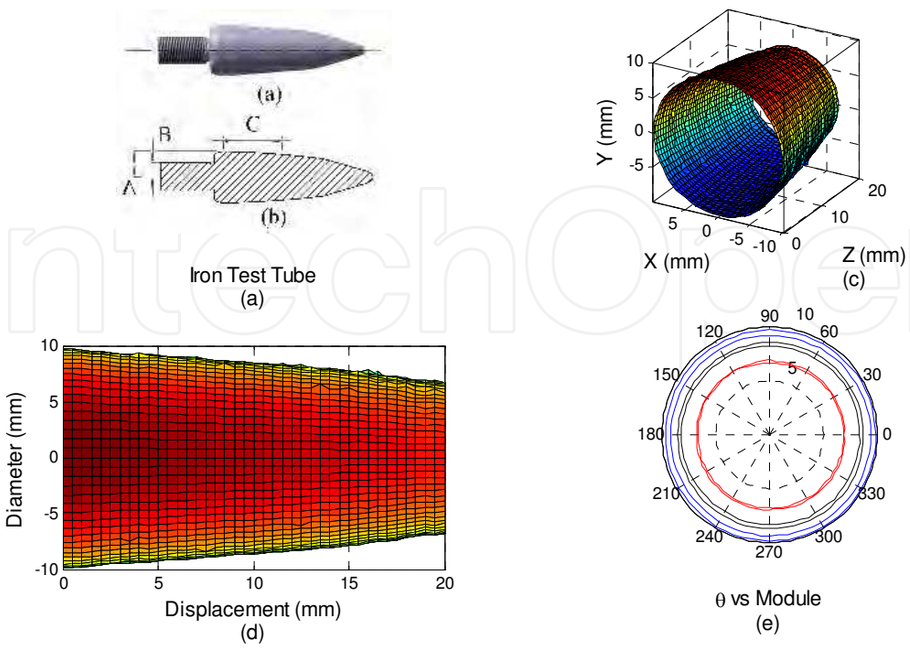

Fig. 22. b)- c) and d) are 3D scan results of a sector of the sample shown in a).

The last example is to show a different configuration in the interferometer system.

With this set-up it is possible to obtain measurement of two sample's face simultaneously employing a third reference surface, which is an advantage over other techniques as the interferometric gauge block, (Decker & Pekelsky, 1997). This is very useful for thickness measurements in opaque samples or where the refraction index is unknown. In figure 23 it is shown a basic Sagnac-Michelson interferometer set-up (Morel & Torga, 2009). This is a ring interferometer type were M_1 is the reference mirror; M_2 and M_3 are the mirrors employed to send the light to each face of the sample (S in the figure 1).

BS_1 and BS_2 are two beam splitters. The light source is a superluminescent diode and the detector system ends in a spectrometer. The reference arm ends in mirror E_1. After BS_2, the two beams are directed to each of the faces of the sample; after their reflections in the sample face and reflection E_1, we obtain three interference signals which let us know the sample thickness. We measure the interference signals in the detector system.

In order to identify the origin of each of the interference signals employed in the measurements, we define D_r as the optical path difference (OPD) between the reference arm and the beam in the ring interferometer when the sample has been removed; D_2 and D_3 represent the OPD between the reference arm and the reflections in each of the sample faces, and D_1 is the OPD between both samples faces.

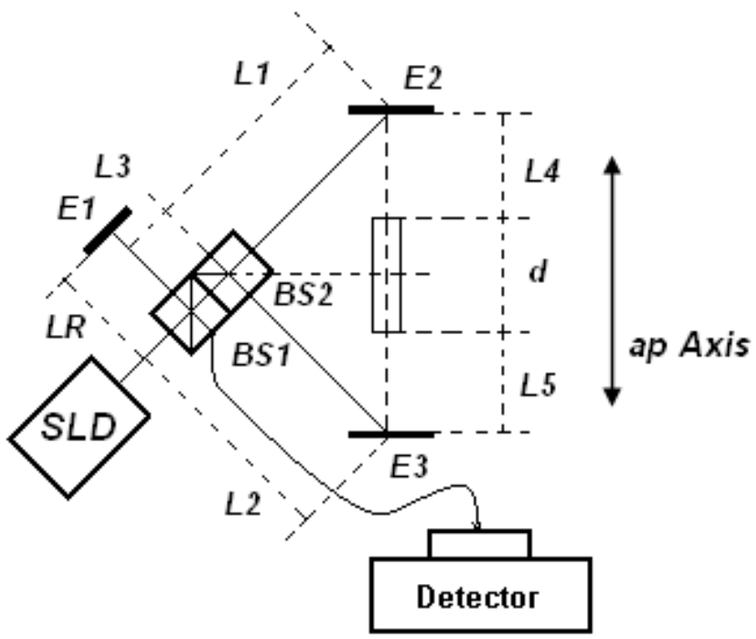

Fig. 23. Sagnac-Michelson interferometer.

The expressions for the different OPD are defined as follow:

$$D_r = \left(L_1 + L_2 + 2L_3 + L_4 + L_5 + d\right) - 2\left(LR\right) \tag{23}$$

$$D_1 = 2\left(L_4 + L_1 + L_3\right) - 2\left(L_5 + L_2 + L_3\right) \tag{24}$$

$$D_2 = 2\left(L_4 + L_1 + L_3\right) - 2\left(LR\right) \tag{25}$$

$$D_3 = 2\left(L_5 + L_2 + L_3\right) - 2\left(LR\right) \tag{26}$$

We showed that it is possible to get the sample thickness (d) with the following relations:

$$d = \left| \frac{\left(D_2 + D_3\right) - 2D_r}{2} \right| \tag{27}$$

As D_2 and D_3 are the OPD between the sample and a reference plane, a lateral displacement of the sample let us obtain the surface topography of each of the faces. From the same curves it is possible to improve the alignment of the sample with the reference plane (in our set-up the mirror E_1).

An example of a typical measurement obtained with this set-up is shown in figure 25. The nominal thickness of each gauge is 1.1 mm and 1.05 mm. Both are positioned so that one side has an exposed step and the other side forms a planar surface. The total lateral displacement in the experiment is about 10 mm. We called e1 to the step between the two gauges; e_3 and e_2 are the thickness of each gauge.

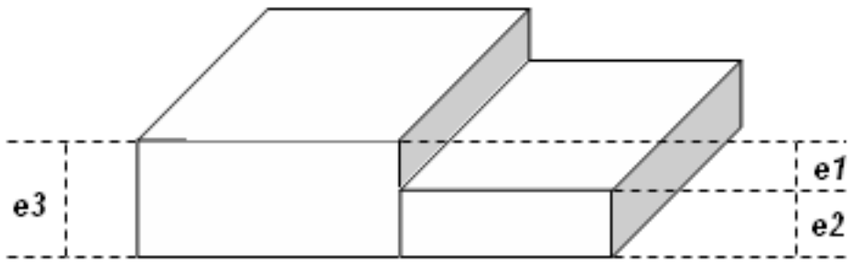

Fig. 24. Schematic of the sample.

In figure 25.a it is shown the profile obtained from the measurement of D_1. Figures 25.b and 25.c show the profiles of both faces of the sample (D_2 and D_3). From these results it is possible to obtain the height of the step (e1 in figure 24) and the thickness of both gauges (e3 and e2 in the figure 24). The slopes of these curves let us to obtain the relative alignment of each of the sample faces with a reference plane and the relative alignment between both gauges.

The values obtained for the gauges thickness are 1091.7 μm and 1047.46 μm, with an average dispersion of 1.32 μm, in very good agreement with the expected value.

There is a dark zone in the curves that appears when the sample presents abrupt changes in surface topography, so the light is scattered in high angles and the collected light intensity is under the detection sensitivity. The optic to focus light on the sample can be selected to minimize dark zone usually lowering the dynamical range of the interferometer.

This method enables simultaneous measurements of physical thickness and refractive group index without any prior knowledge on samples as showed in (Park et al, 2011).

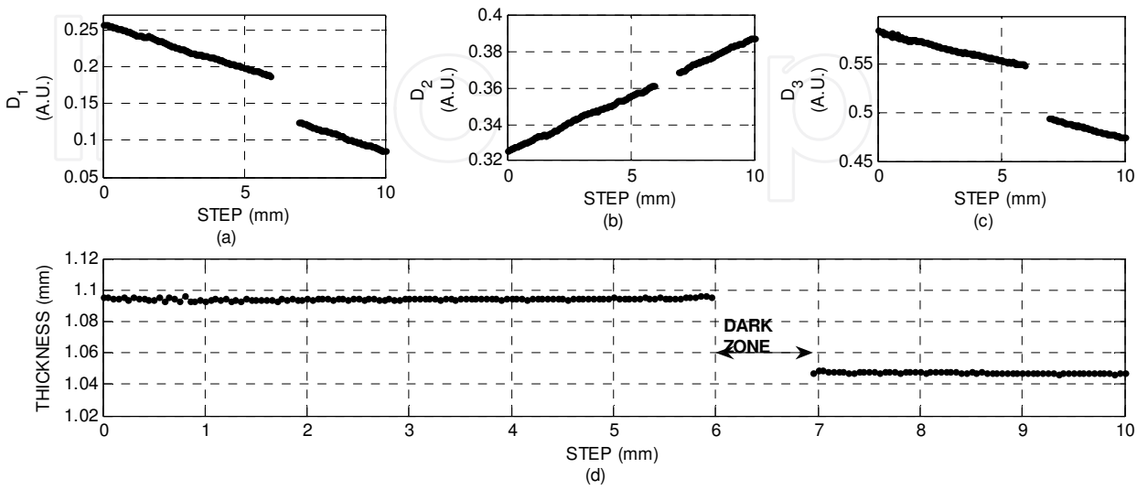

Fig. 25. Surface profiles and thickness obtained from the sample shown in figure 24.

4. Conclusions

In this chapter we present a brief introduction to the theory of low coherence interferometry and the main configurations used nowadays. Then, we focus in giving a detailed analysis of the technique "Spectral domain low coherence interferometry" that offer interesting advantages over alternative methods. We give a description of the limitations and experimental design considerations to take account in the detection of the interference intensity and in the signal processing. We also show how this knowledge is important to improve the information obtained from the images.

At the end we show some experimental results with the intention of giving examples of the enormous potential of this technique, specially in the non- destructive tests area, where we think is nowadays largely unexplored.

5. Acknowledgment

E. Morel and J. Torga are professors at the Universidad Tecnológica Nacional and are members of the Consejo Nacional de Investigaciones Científicas y Técnicas de la República Argentina.

Thanks to Hernán Miranda for his collaboration and special thanks to Pamela Morel for her support and images design.

6. References

Bajraszewski,T; Wojtkowski, M.; Szkulmowski, M.; Szkulmowska, A.; Huber, R. and Kowalczyk A., "Improved spectral optical coherence tomography using optical frequency comb" Opt. Express 16, 4163-4176 (2008). doi:10.1364/OE.16.004163.

Boaz, P.; "A course in digital signal processing" John Wiley & Sons, 1997. ISBN: 978-0-471-14961-3.

Born, M. & Wolf, E. (2002), Cambridge University Press, ISBN 13 978-0-521-64222-4, London, England.

Bruce L. Danielson and C. Y. Boisrobert, "Absolute optical ranging using low coherence interferometry," Appl. Opt. 30, 2975-2979 (1991). doi:10.1364/AO.30.002975.

Choma, M,; Sarunic, M.; Yang, C.; and Izatt, J. "Sensitivity advantage of swept source and Fourier domain optical coherence tomography," Opt. Express 11, 2183-2189 (2003). doi:10.1364/OE.11.002183.

Decker JE, Pekelsky JR. "Gauge block calibration by optical interferometry at the national research council of Canada". Measurement Science Conference Pasadena, California, 23–24 January 1997; NRC Internal Report no. 40002.

Dorrer, C.; Belabas, N.; Likforman, J.; and Joffre, M.; "Spectral resolution and sampling issues in Fourier-transform spectral interferometry," J. Opt. Soc. Am. B 17, 1795-1802 (2000). doi:10.1364/JOSAB.17.001795.

Drexler, W. & Fujimoto, J. "Optical Coherence Tomography: Technology and Applications", Springer Publishing, (2008). ISBN 978-3-540-77549-2, 1400 pages.

Fercher, A.; Hitzenberger, C.; Kamp, G.; El-Zaiat, S.; "Measurement of intraocular distances by backscattering spectral interferometry," Opt.Commun. 117, 43-48,(1995). DOI: 10.1016/0030-4018(95)00119-S.

Fujimoto, J. (2002). Optical Coherence Tomography: Introduction. In: Bouma B E & Tearney G J (eds), Handbook of Optical Coherence Tomography, Marcel Dekker, Inc., New York,USA.

Goode, B. (2009). Optical Coherence Tomography: OCT aims for industrial application, Laser Focus World, Vol 45 (9).

Goodman, J. (1984). Statistical Optics, John Wiley & Sons, ISBN 0-471-01502-4.

Häusler, G. and Lindner, M.; "Coherence radar and spectral radar – new tools for dermatological diagnosis" J. Biomed. Opt. 3, 21-31(1998). doi:10.1117/1.429899.

Huang, D.; Swanson, EA .; Lin, CP.; Schuman, JS .; Stinson, WG .; Chang, W .; Hee, MR .; Flotte, T.; Gregory, K.; Puliafito, CA. and Fuyimoto, J.; "Optical coherence tomography", Science, 22 November 1991:Vol. 254. DOI: 10.1126/ science.1957169.

Hu, Z.; Pan, Y. & Rollins, A.; "Analytical model of spectrometer-based two-beam spectral interferometry," Appl. Opt. 46, 8499-8505 (2007). doi:10.1364/AO.46.008499.

Jeon, M.; Kim, J.; Jung, U.; Lee, C.; Jung, W. and Boppart, S.A.; "Full-range k-domain linearization in spectral-domain optical coherence tomography," Appl. Opt. 50, 1158-1163 (2011). doi:10.1364/AO.50.001158.

Morel, E.N. ; Torga, J.R.; "Dimensional characterization of opaque samples with a ring interferometer", Optics and Lasers in Engineering, Volume 47, Issue 5, May 2009, Pages 607-611, ISSN 01438166.

Leitgeb, R.; Hitzenberger, C. and Fercher, A.; "Performance of fourier domain vs. time domain optical coherence tomography," Opt. Express 11, 889-894 (2003). doi:10.1364/OE.11.000889.

Oppenheim A.V., R.W. Schafer y J.R. Buck Tratamiento de señales en tiempo discreto, Prentice Hall, Madrid (2000). ISBN: 8420529877.

Papoulis, A.; (1962), "The Fourier Integral and its Applications", Mc Graw Hill, June 1, 1962, ISBN-13: 978-0070484474.

Park, S.J.; Park, K.S.; Kim, Y.H. and Lee,*B.H.*; "Simultaneous Measurements of Refractive Index and Thickness by Spectral-Domain Low Coherence Interferometry Having Dual Sample Probes", ieee Photonics Technology Letters, 1041-1135, vol. 23, no. 15, august 1, 2011. DOI: 10.1109/lpt.2011.2155642.

Schmitt, J. ;(1999). "Optical coherence tomography (OCT): a review" IEEE Journal of Selected Topics in Quantum Electronics", Vol. 5, No. 4, July/August. DOI: 10.1109/2944.796348. ISSN: 1077-260X.

Swanson, E. "OCT News". Available from: www.octnews.org.

Takada, K.; Yokohama, I.; Chida, K. & Noda J.; (1987). "New measurement system for fault location in optical waveguide devices based on an interferometric technique," Appl. Opt. 26, 1603-1606. doi:10.1364/AO.26.001603.

Vakhtin, A.; Peterson, K.; Wood, W. & Kane, D. (2003), "Differential spectral interferometry: an imaging technique for biomedical applications," Opt. Lett. 28, 1332-1334. doi:10.1364/OL.28.001332.

Wang, H.; Pan, Y.; and Rollins A.; "Extending the effective imaging range of Fourier-domain optical coherence tomography using a fiber optic switch," Opt. Lett. 33, 2632-2634 (2008). doi:10.1364/OL.33.002632.

Wang, Z.; Yuan, Z.; Wang, H.; and Pan, Y.; "Increasing the imaging depth of spectral-domain OCT by using interpixel shift technique," Opt. Express 14, 7014-7023 (2006). doi:10.1364/OE.14.007014.

Wieasuer, K.; Pircher, M.; Götzinger, E.; Bauer, S.; Engelke, R.; Ahrens, G.; Grützner, G.; Hitzenberger, C. & Stifter, D. (2005), "En-face scanning optical coherence tomography with ultra-high resolution for material investigation," Opt. Express 13, 1015-1024.

Wiesner M.; Ihlemann, J.; Müller, H.; Lankenau, E. & Hüttmann, G. (2010). "Optical coherence tomography for process control of laser micromachining"; Review of Scientific Instruments, Vol. 81, Iss. 3, pg. 033705.

Wojtkowski, M. ; Leitgeb, R.; Kowalczyk, A.; Bajraszewski, T. and Fercher, A.; "In vivo human retinal imaging by Fourier domain optical coherence tomography", J. Biomed. Opt. 7, 457 (2002); doi:10.1117/1.1482379.

Wojtkowski, M.; Bajraszewski, T.; Targowski, P.; Kowalczyk, A.; "Real-time in-vivo ophthalmic imaging by ultrafast spectral interferometry" Proc. SPIE 4956, 4956-11 (2003). doi:10.1364/OE.11.000889.

Youngquist, R; Sally Carr, & Davies D. (1987 "Performance of fourier domain vs. time domain optical coherence tomography," Opt. Express 11, 889-894 (2003). doi:10.1364/OE.11.000889.

Yun, S.; Tearney, G.; Bouma, B.; Park, B. and Boer, J.; "High-speed spectral-domain optical coherence tomography at 1.3 μm wavelength," Opt. Express 11, 3598-3604 (2003). doi:10.1364/OE.11.003598.

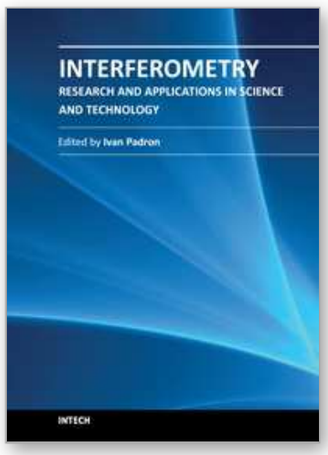

Interferometry - Research and Applications in Science and Technology

Edited by Dr Ivan Padron

ISBN 978-953-51-0403-2
Hard cover, 462 pages
Publisher InTech
Published online 21, March, 2012
Published in print edition March, 2012

This book provides the most recent studies on interferometry and its applications in science and technology. It is an outline of theoretical and experimental aspects of interferometry and their applications. The book is divided in two sections. The first one is an overview of different interferometry techniques and their general applications, while the second section is devoted to more specific interferometry applications comprising from interferometry for magnetic fusion plasmas to interferometry in wireless networks. The book is an excellent reference of current interferometry applications in science and technology. It offers the opportunity to increase our knowledge about interferometry and encourage researchers in development of new applications.

InTech Europe
University Campus STeP Ri
Slavka Krautzeka 83/A
51000 Rijeka, Croatia
Phone: +385 (51) 770 447
Fax: +385 (51) 686 166
www.intechopen.com

InTech China
Unit 405, Office Block, Hotel Equatorial Shanghai
No.65, Yan An Road (West), Shanghai, 200040, China
中国上海市延安西路65号上海国际贵都大饭店办公楼405单元
Phone: +86-21-62489820
Fax: +86-21-62489821

IntechOpen